

# Periodic Vibration Gaussian: Dynamic Urban Scene Reconstruction and Real-time Rendering

Yurui Chen<sup>1\*</sup> Chun Gu<sup>1\*</sup> Junzhe Jiang<sup>1</sup> Xiatian Zhu<sup>2</sup> Li Zhang<sup>1✉</sup>

<sup>1</sup> Fudan University <sup>2</sup> University of Surrey

<https://fudan-zvg.github.io/PVG>



(a) Dynamic scene

(b) Remove the dynamic

Figure 1. Our proposed **Periodic Vibration Gaussian** is crafted to effectively and uniformly capture both the static and dynamic elements of a large, dynamic urban scene. (a) It not only reconstructs a *dynamic* urban scene but also enables *real-time rendering*, while efficiently isolating dynamic components from the intricacies of the highly unconstrained and complex scene. (b) This capability facilitates flexible manipulation, such as the removal of dynamic scene elements.

## Abstract

*Modeling dynamic, large-scale urban scenes is challenging due to their highly intricate geometric structures and unconstrained dynamics in both space and time. Prior methods often employ high-level architectural priors, separating static and dynamic elements, resulting in suboptimal capture of their synergistic interactions. To address this challenge, we present a unified representation model, called **Periodic Vibration Gaussian** (PVG). PVG builds upon the efficient 3D Gaussian splatting technique, originally designed for static scene representation, by introducing periodic vibration-based temporal dynamics. This innovation enables PVG to elegantly and uniformly represent the characteristics of various objects and elements in dynamic urban scenes. To enhance temporally coherent representation learning with sparse training data, we introduce a novel flow-based temporal smoothing mechanism and a position-aware adaptive control strategy. Extensive experiments on Waymo Open Dataset [29] and KITTI benchmarks [12] demonstrate that PVG surpasses state-of-the-art alternatives in both reconstruction and novel view synthesis for both dynamic and static scenes. Notably, PVG achieves this without relying on manually labeled object bounding boxes or expensive optical flow estimation. Moreover, PVG ex-*

*hibits 50/6000-fold acceleration in training/rendering over the best alternative.*

## 1. Introduction

The geometric reconstruction of extensive urban spaces, such as streets and cities, has played a pivotal role in applications like digital maps, auto-navigation, and autonomous driving [6, 12, 29]. Our world is inherently dynamic and complex in both spatial and temporal dimensions. Despite advancements in scene representation techniques like Neural Radiance Fields (NeRFs) [13, 27, 40], which primarily focus on static scenes, they overlook more challenging dynamic elements.

Recent approaches to model dynamic scenes include NSG [22], which decomposes dynamic scenes into scene graphs and learns a structured representation. PNF [16] further decomposes scenes into objects and backgrounds, incorporating a panoptic segmentation auxiliary task. However, scalability issues arise in real-world scenarios, where obtaining accurate object-level supervisions (e.g., 3D object boxes, segmentation masks) is challenging, and explicitly representing each object linearly increases model complexity with the number of objects.

SUDS [33] later proposes using optical flow to relax the stringent requirement of object labeling in a three-branch architecture for separately modeling static and dynamic elements and the environmental factors of a scene. Despite

\*Equally contributed.

✉Li Zhang (lizhangfd@fudan.edu.cn) is the corresponding author with School of Data Science, Fudan University.

adopting implicit NeRF representation, these methods suffer from low efficiency in both training and rendering, posing a significant bottleneck for large-scale scene rendering and reconstruction. Additionally, manually separating constituent parts introduces design complexity and limits the ability to capture intrinsic correlations and interactions.

To overcome the identified limitations, this paper introduces a novel dynamic scene representation method termed **Periodic Vibration Gaussian** (PVG). This approach provides a unified representation of both static and dynamic elements within a scene through a single formulation. Building upon the efficient 3D Gaussian Splatting technique [14], originally devised for static scene representation, we incorporate periodic vibration-based temporal dynamics. This modification allows for a cohesive representation of static and dynamic scene elements with explicit motion properties such as velocity and staticness. To improve the temporal continuity in representation learning with typically limited training data, we introduce a scene flow-based temporal smoothing mechanism and a position-aware point adaptive control strategy.

Our **contributions** are summarized as follows: **(i)** Introduction of the very first unified representation model, Periodic Vibration Gaussian (PVG), for large-scale dynamic urban scene reconstruction. In contrast to previous NeRF-based solutions, PVG employs the 3D Gaussian Splatting paradigm, uniquely extending it to elegantly represent dynamic scenes. This is accomplished by seamlessly integrating periodic vibration-based temporal dynamics into the conventional 3D Gaussian Splatting formulation. **(ii)** Development of a scene flow-based temporal smoothing mechanism to enhance the temporal continuity of representation and a position-aware point adaptive control strategy for unbounded urban scenes. **(iii)** Extensive experiments on two large benchmarks (KITTI and Waymo) demonstrate that PVG outperforms all previous state-of-the-art alternatives in novel view synthesis. Moreover, it provides significant efficiency benefits in both training and rendering processes, achieving a **50**-fold acceleration in training and a remarkable **6000**-fold acceleration in rendering compared to the leading competitor, SUDS [33].

## 2. Related work

**Neural rendering** In the domain of novel view synthesis, Neural Radiance Fields (NeRF) [20] have emerged as a noteworthy approach. NeRF employs a coordinate-based multi-layer perception representation of 3D scenes, leveraging volumetric rendering and the spatial smoothness of multi-layer perception to generate high-quality novel views. However, its implicit nature comes with significant drawbacks, including slow training and rendering speeds, as well as high memory usage.

To tackle these challenges, several studies have proposed

solutions to enhance training speed. Techniques such as voxel grids [28], hash encoding [21], and tensor factorization [8, 9] have been explored. Others have focused on improving rendering speed by transforming implicit volumes into explicit textured meshes, as demonstrated in works like [10, 26, 42]. Additionally, endeavors such as [3–5, 34] aim to enhance rendering quality by addressing issues like antialiasing and reflection modeling. More recently, 3D Gaussian Splatting (3DGS) introduced an innovative point-based 3D scene representation, seamlessly integrating the high-quality volume rendering principles of NeRF [20] with the swift rendering speed characteristic of rasterization.

**Dynamic scene models** Reconstructing dynamic scenes poses distinctive challenges, particularly in effectively handling temporal correlations across various time steps. Expanding on the accomplishments of NeRF [20], several extensions have been proposed to tailor NeRF to dynamic scenarios. In one research direction, certain studies [2, 7, 11, 17, 35] introduce time as an additional input to the radiance field, treating the scene as a 6D plenoptic function. However, this approach couples positional variations induced by temporal dynamics with the radiance field, lacking geometric priors about how time influences the scene. An alternative approach [1, 19, 23–25, 31, 37] focuses on modeling the movement or deformation of specific static structures, assuming that the dynamics arise from these static elements within the scene. Point-based methods [1, 19, 37] have shown promise in addressing the challenges of reconstructing dynamic scenes due to their flexibility. Building upon the progress in 3D Gaussian splatting, recent works [19, 37] propose the use of a set of deformable 3D Gaussians for optimization across different timestamps.

**Urban scene reconstruction** NeRF-based techniques have shown their efficacy in autonomous driving scenarios [12, 29]. One research avenue has focused on enhancing the modeling of static street scenes by utilizing scalable representations [18, 27, 30, 32], achieving high-fidelity surface reconstruction [13, 27, 36], and incorporating multi-object composition [40]. However, these methods face difficulties in handling dynamic elements commonly encountered in autonomous driving contexts. Another research direction seeks to address these challenges. Notably, these techniques require additional input, such as leveraging panoptic segmentation to refine the dynamics of reconstruction [16]. Moreover, in [22], scene graphs are employed to decompose dynamic multi-object scenes, while in [41], neural shape priors are learned for completing dynamic object reconstructions. In [38] foreground instances and background environments are decomposed. However, they all need manually annotated bounding boxes. In [33], a scalable hash table is proposed for large-scale dynamic scenes, relying on an off-the-shelf 2D optical flow estimator to track dynamic actors.

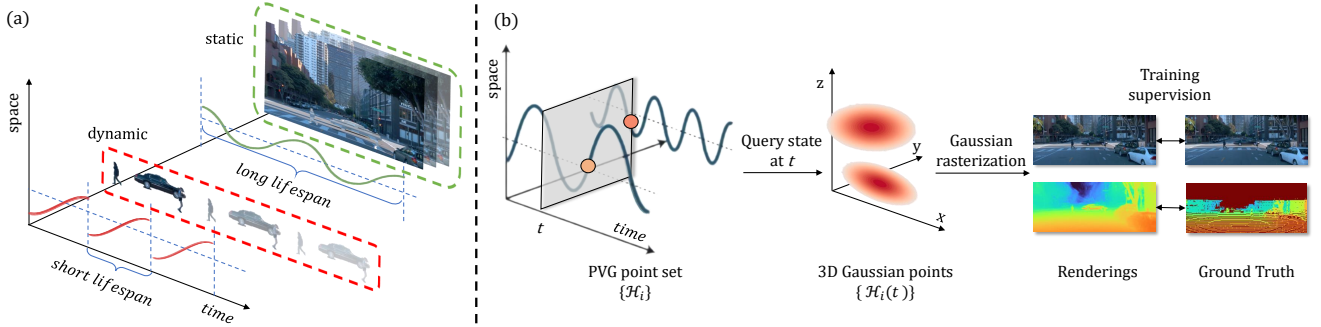


Figure 2. (a) Dynamic and static can be expressed uniformly through different Periodic Vibration Gaussian points with different lifespan. Our model can be trained to differentiate between dynamic and static on its own. (b) Our training pipeline.

In this paper, we present an elegant extension of 3D Gaussian Splatting [14] with the additional time dimension to handle the complexities of dynamic scenes. Our model provides a uniform, efficient representation, excelling in reconstructing dynamic, large-scale urban scenes without the dependence on manual annotations or pre-trained models.

### 3. Method

Utilizing the sequentially acquired and calibrated multi-sensor data, encompassing a set of images  $\mathcal{I}$ , each captured by cameras equipped with corresponding intrinsic matrices  $\mathbf{I}$  and extrinsic matrices  $\mathbf{E}$ , alongside their respective capture timestamps  $t$ , collectively represented as  $\{\mathcal{I}_i, t_i, \mathbf{E}_i, \mathbf{I}_i | i = 1, 2, \dots, N_c\}$ , and the spatial coordinates of LiDAR point clouds annotated with timestamps  $\{(x_i, y_i, z_i, t_i) | i = 1, 2, \dots, N_l\}$ , our research aims to achieve precise 3D reconstruction and synthesize novel viewpoints at any desired timestamp  $t$  and camera pose  $[\mathbf{E}_o, \mathbf{I}_o]$ . To this end, our framework is meticulously engineered to approximate a rendering function  $\hat{\mathcal{I}} = \mathcal{F}_{\theta}(\mathbf{E}_o, \mathbf{I}_o, t)$ .

#### 3.1. Preliminary

3D Gaussian Splatting (3DGS) [14] utilizes a collection of 3D Gaussians to represent a scene. Through a tile-based rasterization process, 3DGS facilitates real-time alpha blending of numerous Gaussians. The scene is modeled by a set of points  $\{P_i\}$ , where each point  $P$  is linked to a mean  $\mu \in \mathbb{R}^3$ , a covariance matrix  $\Sigma \in \mathbb{R}^{3 \times 3}$ , an opacity  $o$ , and a color  $\mathbf{c}$ . These attributes collectively define the point's influence within the 3D space as:

$$G(\mathbf{x}) = e^{-\frac{1}{2}(\mathbf{x}-\boldsymbol{\mu})^T \boldsymbol{\Sigma}^{-1} (\mathbf{x}-\boldsymbol{\mu})}. \quad (1)$$

To create an image from a particular viewpoint, 3DGS maps each Gaussian point onto the image plane, yielding a collection of 2D Gaussians. Calculating the means of these projected Gaussians is straightforward. However, determin-

ing the formulation for the projected variance involves

$$\Sigma' = JW \Sigma W^T J^T, \quad (2)$$

where  $W$  and  $J$  are the view transform matrix and Jacobian of the nonlinear projective transform matrix, respectively. Sorting the Gaussians according to their depth in camera space, we can query the attributes of each 2D Gaussian and facilitate the subsequent volume rendering process to determine the color of each pixel:

$$C = \sum_{i=1}^N T_i \alpha_i \mathbf{c}_i \text{ with } T_i = \prod_{j=1}^{i-1} (1 - \alpha_j), \quad (3)$$

where  $\alpha$  is derived through the product of the opacity  $o$  and the contribution from the 2D covariance calculated using  $\Sigma'$  and the corresponding pixel coordinates in the image space.

The covariance matrix holds a meaningful interpretation when it is positive semi-definite. In the context of 3DGS, it is decomposed into a scaling matrix, denoted as a diagonal matrix represented by  $\mathbf{s} \in \mathbb{R}^3$ , and a rotation matrix represented by a unit quaternion  $\mathbf{q}$ .

The differentiable rendering function for a new view of a scene containing  $N$  points is expressed as

$$\hat{\mathcal{I}} = \text{Render}(\{\mathcal{C}_i | i = 1, 2, \dots, N\}; \mathbf{E}, \mathbf{I}), \quad (4)$$

where  $\hat{\mathcal{I}}$  is the rendered image, and  $\mathbf{E}$  and  $\mathbf{I}$  denote the camera extrinsic and intrinsic matrices, respectively. The training of the model entails optimizing the parameter set for each point, represented as  $\mathcal{C} = \{\boldsymbol{\mu}, \mathbf{q}, \mathbf{s}, o, \mathbf{c}\}$ .

**Flexible rendering** This rendering method can tackle different targets, like depth and opacity, by replacing the color  $\mathbf{c}$  in Eq. (3). For example, the depth map can be computed as:  $\sum_{i=1}^N T_i \alpha_i z_i$ , where  $z_i$  represents the distance of the center of a Gaussian point from the image plane.

**Limitation** The 3D Gaussian Splatting model represents static points in a scene, lacking the ability to capture dynamic changes over time, essential for modeling dynamic urban scenes. To address this limitation, we propose the Periodic Vibration Gaussian model.

### 3.2. Periodic Vibration Gaussian

Our Periodic Vibration Gaussian (PVG) model exhibits several distinctive features:

**Dynamics introduction:** We introduce the concept of *life peak*, denoted as  $\tau$ , which represents the point’s moment of maximum prominence over time. The motivation behind this concept is to assign a distinct lifespan to each Gaussian point, defining when it actively contributes and to what degree. This fundamentally infuses a dynamic nature into the model, enabling variations in the collection of Gaussian points that influence the rendering of the scene over time.

**Periodic vibration:** We modify the traditional 3D Gaussian’s mean  $\mu$  and opacity  $o$  to be time-dependent functions centered around the life peak  $\tau$ , denoted as  $\tilde{\mu}(t)$  and  $\tilde{o}(t)$ . Both functions peak at  $\tau$ . This adaptation empowers the model to effectively capture dynamic motions, enabling each point to adjust based on temporal changes.

Formally, our model, denoted as  $\mathcal{H}$ , is expressed as:

$$\mathcal{H}(t) = \{\tilde{\mu}(t), \mathbf{q}, \mathbf{s}, \tilde{o}(t), \mathbf{c}\}, \quad (5)$$

$$\tilde{\mu}(t) = \mu + \mathbf{A} \cdot \sin\left(\frac{2\pi(t - \tau)}{l}\right), \quad (6)$$

$$\tilde{o}(t) = o \cdot e^{-\frac{1}{2}(t - \tau)^2 \beta^{-2}}, \quad (7)$$

where  $\tilde{\mu}(t)$  represents the vibrating motion centered at  $\mu$  occurring at the life peak  $\tau$ , and  $\tilde{o}(t)$  denotes the vibrating opacity, which decays away from the peak  $\tau$  with a decay rate inversely proportional to  $\beta$ . Notably, the parameter  $\beta$  governs the lifespan around  $\tau$ , with larger values indicating bigger lifespans. The parameter  $l$  represents the cycle length, serving as the scene prior. The parameter  $\mathbf{A} \in \mathbb{R}^3$  signifies the vibrating direction. Therefore, the learnable parameters of our model  $\mathcal{H}$  include  $\{\mu, \mathbf{q}, \mathbf{s}, o, \mathbf{c}, \tau, \beta, \mathbf{A}\}$ .

In particular, we express the mean vector (position)  $\tilde{\mu}(t)$  through periodic vibrations, providing a cohesive framework for both static and dynamic patterns. To enhance clarity, we introduce the *staticness coefficient*  $\rho = \frac{\beta}{l}$ , which quantifies the degree of staticness exhibited by a PVG point and is also associated with the point’s lifespan. Periodic vibration facilitates convergence around  $\mu$  when  $\rho$  is large. This is due to the bounded nature of  $\tilde{\mu}(t)$  by  $\mathbf{A}$  and the fact that  $\mathbb{E}[\tilde{\mu}(t)] = \mu$  holds for any time interval with a length that is a multiple of  $l$ , independent of  $\mathbf{A}$ .

We note that the 3DGS represents a particular case of PVG in which  $\mathbf{A} = \mathbf{0}$  and  $\rho = +\infty$ . PVGs with large  $\rho$  effectively capture the static aspects in a scene, provided that  $\|\mathbf{A}\|$  remains within a reasonable range.

The ability of our PVG to represent the dynamic aspects of a scene is particularly evident in points with small  $\rho$ . Points approaching  $\rho \rightarrow 0$  manifest by appearing and disappearing almost instantaneously, executing linear movements around the time  $\tau$ . As time progresses, these

points undergo oscillations, with some vanishing and others emerging. At a specific timestamp  $t$ , dynamic objects are more likely to be predominantly represented by points with  $\tau$  close to  $t$ . In essence, different points take charge of representing dynamic objects at distinct timestamps.

Conversely, the static components of a scene can be effectively represented by points exhibiting large  $\rho$ . Introducing a threshold on  $\rho$  enables us to discern whether a point represents dynamic elements (see Figure 1(b)).

It is crucial to emphasize that at any given time  $t$ , our model takes the form of a specific 3D Gaussian model, represented by  $\mathcal{H}(t)$ . We train a collection of PVG points, denoted as  $\{\mathcal{H}_i\}$ , to effectively portray a dynamic scene. The rendering process is then executed as:

$$\hat{\mathcal{I}} = \text{Render}(\{\mathcal{H}_i(t) | i = 1, \dots, N_H\}; \mathbf{E}, \mathbf{I}), \quad (8)$$

where  $N_H$  represents the number of PVG points in a scene. Our training pipeline can be seen in Figure 2.

### 3.3. Position-aware point adaptive control

The conventional adaptive control method, as introduced in [14], treating each Gaussian point uniformly, proves inadequate for urban scenes. This is mainly attributed to the substantial distance of the mean vector (position)  $\mu$  for most points from the center of the unbounded scene. To faithfully represent the scene with fewer points without sacrificing accuracy, we advocate utilizing larger points for distant locations and smaller points for nearby areas.

Assuming camera poses are centered, the inclusion of the scale factor  $\gamma(\mu)$  as defined below is essential for effective control over each PVG point:

$$\gamma(\mu) = \begin{cases} 1 & \text{if } \|\mu\|_2 < 2r \\ \|\mu\|_2/r - 1 & \text{if } \|\mu\|_2 \geq 2r, \end{cases} \quad (9)$$

where  $r$  denotes the scene radius (i.e., the scene scope). Specifically, we employ a densification strategy for a PVG  $\mathcal{H}(t)$  when its backward gradient on view space surpasses a specified threshold. We opt to clone the PVG if  $\max(\mathbf{s}) \leq g \cdot \gamma(\mu)$ , with  $g$  serving as the threshold for scale. Conversely, if this condition is not met, we initiate a split operation. Additionally, we undertake pruning of points with  $\max(\mathbf{s}) > b \cdot \gamma(\mu)$ , employing  $b$  as the scale threshold to discern whether a given PVG is excessively large.

### 3.4. Model training

**Temporal smoothing by scene flow** Reconstructing dynamic scenes in autonomous driving poses a significant challenge, primarily attributed to the sparse data in terms of both views and timestamps, as well as the unconstrained variations across frames. Specifically, in PVG, individual points encompass only a narrow time window, resulting in constrained training data and an increased susceptibility to

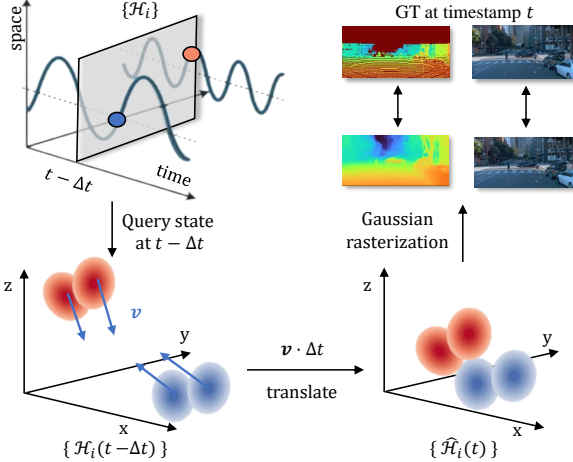


Figure 3. Our scene flow-based temporal smoothing mechanism. We query the status of PVG point set at  $t - \Delta t$  and translate each point with its 3D flow distance  $v \cdot \Delta t$ , we further render the translated set of points to do the supervision at timestamp  $t$ .

overfitting. To address this, we capitalize on the inherent dynamic properties of PVG, which establish connections between the states of consecutive observations.

Instead of using external flow estimation, we introduce the ***scene velocity*** metric as:

$$\mathbf{v} = \frac{d\tilde{\mu}(t)}{dt} \Big|_{t=\tau} \cdot \exp(-\frac{\rho^2}{2}) = \frac{2\pi\mathbf{A}}{l} \cdot \exp(-\frac{\rho^2}{2}). \quad (10)$$

This metric is bounded as it satisfies that  $\lim_{\rho \rightarrow \infty} \mathbf{v} = \mathbf{0}$ , and  $\lim_{\rho \rightarrow 0} \mathbf{v} = \frac{2\pi\mathbf{A}}{l}$ .

In practical scenarios, dynamic objects often maintain a constant speed within a short time interval. This observation leads to the emergence of a linear relationship between consecutive states of PVG.

Formally, consider two adjacent timestamps,  $t_1$  and  $t_2$  ( $t_1 < t_2$ ) with their respective states represented as  $\{\mathcal{H}_i(t_1)\}$  and  $\{\mathcal{H}_i(t_2)\}$ . These states are linearly connected by a ***scene flow translation*** for each point, denoted as  $\Delta\mu = \mathbf{v} \cdot (t_2 - t_1) = \mathbf{v}\Delta t$ . Specifically, we estimate the underlying state of  $\mathcal{H}(t_2)$  as:

$$\hat{\mathcal{H}}(t_2) = \{\tilde{\mu}(t_1) + \mathbf{v} \cdot \Delta t, \mathbf{q}, \mathbf{s}, \tilde{o}(t_1), \mathbf{c}\}. \quad (11)$$

It is important to highlight that this estimation process is applied to each individual PVG point. A visual representation of this estimation is illustrated in Figure 3.

We utilize estimated states to improve model training. Specifically, we assign a probability of  $\eta$  to set  $\Delta t$  as 0 (indicating no estimation), and for the remaining probability, we randomly sample  $\Delta t$  from a uniform distribution  $U(-\delta, +\delta)$ . In the latter case, we replace  $\mathcal{H}$  (Eq. (8)) with  $\hat{\mathcal{H}}$  during training. This modification enables the model to grasp the underlying dynamics, fostering a more consistent representation without imposing a significant increase

in computational demands. By adopting this approach, we improve temporal coherence and consistency, thereby alleviating the challenges posed by sparse data and the risk of overfitting.

**Sky refinement** To handle the high-frequency details in the sky, we utilize a high-resolution environment cube map  $f_{sky}(d) = c_{sky}$ . The final color is articulated as  $C_f = C + (1 - O)f_{sky}(d)$ , where  $O = \sum_{i=1}^{N_H} T_i \alpha_i$  represents the rendered opacity. During the training phase, we incorporate random perturbations to the ray direction  $d$  within its unit pixel length to enhance anti-aliasing.

**Objective** Our objective loss function is formulated as:

$$\mathcal{L} = (1 - \lambda_r)\mathcal{L}_1 + \lambda_r\mathcal{L}_{ssim} + \lambda_d\mathcal{L}_d + \lambda_o\mathcal{L}_o + \lambda_v\mathcal{L}_v, \quad (12)$$

where  $\mathcal{L}_1$  and  $\mathcal{L}_{ssim}$  are L1 and SSIM loss [14] for supervision of RGB rendering.

The term  $\mathcal{L}_d = \frac{1}{hw} \sum \|\mathcal{D}^s - \mathcal{D}\|_1$  is a depth loss for geometry awareness, where  $\mathcal{D}^s$  is a sparse inverse depth map generated by projecting the LiDAR points to the camera plane,  $\mathcal{D}$  denotes the inverse of the rendered depth map, and  $h$  and  $w$  denote the rendering spatial size.

The term  $\mathcal{L}_o = -\frac{1}{hw} \sum O \cdot \log O - \frac{1}{hw} \sum M_{sky} \cdot \log(1 - O)$  is the opacity loss where  $M_{sky}$  is the sky mask estimated by a pretrained segmentation model [39]. This loss aims to drive the opacity values towards either 0 (representing a transparent sky) or 1. Specifically, it regularizes opacity to 0 for predicted sky pixels.

The last term  $\mathcal{L}_v = \frac{1}{hw} \sum \|\mathcal{V}\|_1$  is the sparse velocity loss where  $\mathcal{V}$  is the rendered velocity  $\mathbf{v}$  map. This loss not only leads to a sparse  $\|\mathbf{A}\|$  but also encourages larger  $\beta$  (corresponding to static scene components). The rationale behind this is that most elements of a scene are static.

## 4. Experiments

In this section, we provide quantitative analyses comparing our approach with the state-of-the-art methods. Initially, we describe our experimental setup in Section 4.1. Subsequent to this, in Section 4.2, we detail our experiments conducted on Waymo Open Dataset [29] and KITTI benchmark [12] to affirm the superiority of our approach in managing street-level scenes. Lastly, in Section 4.3, we offer an ablation study detailing the various components of our model and certain regularizations employed during training.

### 4.1. Experiment setup

**Competitors** For dynamic scenes, we evaluate our method alongside S-NeRF [40], StreetSurf [13], Mars [38], 3DGS [14], NSG [22] and SUDS [33]. In line with previous methods, we conduct evaluations on both image reconstruction and novel view synthesis tasks, selecting every fourth timestamp from each camera as the test set for novel view synthesis. Although our primary focus is on dynamic



Figure 4. Qualitative comparison of dynamic reconstruction with baselines. It can be clearly seen that our method shows higher rendering quality compared to the baselines.



Figure 5. Novel view synthesis on static scene on Waymo.

scenes, to be fair, we also provide a quantitative comparison with methods [13, 14, 40] tailored for static scenes. This is to demonstrate our model’s superiority at uniformly managing both static and dynamic environments.

**Implementation details** For points initialization, we sample  $6 \times 10^5$  LiDAR points,  $2 \times 10^5$  near points whose distance to the origin is uniformly sampled from  $(0, r)$ ,  $2 \times 10^5$  far points whose inverse distance is uniformly sampled from  $(0, 1/r)$ , where  $r$  is the foreground radius different across scenes, around 30 meters.  $\beta$  is set to 0.3,  $\mathbf{A}$  is set to  $\mathbf{0}$ . We employ the Adam optimizer [15] and maintain a similar learning rate for most parameters as the original 3DGS implementation while we adjust the learning rate of the amplitude  $\mathbf{A}$ , opacity decaying  $\beta$  and opacity  $o$  to  $3 \times 10^{-5}$ , 0.02 and 0.005 respectively. Regarding the densification schedule, we set the image space densification threshold to  $1.7 \times 10^{-4}$  and reset the opacity of Gaussians to 0.01 every 3,000 iterations to remove superfluous points. For regularization, we use coefficients  $\lambda_r = 0.2$ ,  $\lambda_d = 0.1$ ,  $\lambda_o = 0.05$

and  $\lambda_v = 0.01$ . For scene flow-based training strategy, we uniformly sample time intervals  $\Delta t$  from a 1.5 frame span in the camera sequence with a probability  $\eta = 0.5$ . We set the cube map resolution to 1024 to capture the high-frequency details in the sky. The training process commences from a downsampled scale of 16, which is then gradually increased every 5,000 iterations. We conduct all experiments on a single NVIDIA RTX A6000 GPU for a total of 30,000 iterations which takes about an hour to yield the final results, and the rendering speed can achieve 50 FPS. We rescale the time interval between two consecutive frames to 0.02 and fix  $l = 0.2$ . As shown in Figure 1, ***we remove the PVG points whose  $\rho < 1$  to preserve the static part of the scene.***

**Metrics** Consistent with SUDS [33], we present our results using PSNR, SSIM, and LPIPS metrics to showcase the capability of the Periodic Vibration Gaussian model in image reconstruction and novel view synthesis.

Table 1. Quantitative results of image reconstruction and novel view synthesis of dynamic scenes on Waymo and KITTI. Our method surpass the baselines methods [13, 14, 22, 33, 38, 40] in PSNR, SSIM and LPIPS.

	Waymo Open Dataset						KITTI							
	FPS	Image reconstruction			Novel view synthesis			FPS	Image reconstruction			Novel view synthesis		
		PSNR $\uparrow$	SSIM $\uparrow$	LPIPS $\downarrow$	PSNR $\uparrow$	SSIM $\uparrow$	LPIPS $\downarrow$		PSNR $\uparrow$	SSIM $\uparrow$	LPIPS $\downarrow$	PSNR $\uparrow$	SSIM $\uparrow$	LPIPS $\downarrow$
S-NeRF [40]	0.0014	19.67	0.528	0.387	19.22	0.515	0.400	0.0075	19.23	0.664	0.193	18.71	0.606	0.352
StreetSurf [13]	0.097	27.00	0.850	0.361	21.83	0.776	0.416	0.37	24.14	0.819	0.257	22.48	0.763	0.304
3DGS [14]	<b>63</b>	27.99	0.866	0.293	25.08	0.822	0.319	<b>125</b>	21.02	0.811	0.202	19.54	0.776	0.224
NSG [22]	0.032	24.08	0.656	0.441	21.01	0.571	0.487	0.19	26.66	0.806	0.186	21.53	0.673	0.254
SUDS [33]	0.008	28.83	0.805	0.289	21.83	0.656	0.405	0.04	28.31	0.876	0.185	22.77	0.797	0.171
Mars [38]	0.030	21.81	0.681	0.430	20.69	0.636	0.453	0.31	27.96	0.900	0.185	24.23	0.845	0.160
PVG (Ours)	50	<b>32.46</b>	<b>0.910</b>	<b>0.229</b>	<b>28.11</b>	<b>0.849</b>	<b>0.279</b>	59	<b>31.54</b>	<b>0.927</b>	<b>0.083</b>	<b>26.63</b>	<b>0.885</b>	<b>0.127</b>
PVG (5cam)	41	<b>32.05</b>	<b>0.895</b>	<b>0.252</b>	<b>27.50</b>	<b>0.828</b>	<b>0.312</b>	-	-	-	-	-	-	-

## 4.2. Comparison with state of the art

**Results on Waymo** The Waymo Open Dataset encompasses over 1,000 driving segments, each with a duration of 20 seconds, recorded using five high-resolution LiDARs and five cameras facing the front and sides.

In our experiments, we utilize the three frontal cameras to assess performance on four challenging dynamical scenes, chosen due to their substantial movement. Table 1 displays the average error metrics across these selected dynamic scenes for both image reconstruction and novel view synthesis tasks. Our model markedly outperforms baselines [13, 14, 22, 33, 38, 40] across all metrics in both tasks. Specifically, for the image reconstruction task, we note a 12.6% increase in PSNR, 13.0% in SSIM, and a 20.8% decrease in LPIPS compared to the leading SUDS [33] baseline. These enhancements are visually corroborated in Figure 4, where our method faithfully captures both static and dynamic elements with remarkable detail. For novel view synthesis, our technique synthesizes high-quality views of unseen timestamps and also significantly surpasses the best SUDS performance by 28.8% in PSNR, 29.4% in SSIM, and 31.1% in LPIPS. Noteworthy is our method’s efficiency, completing the entire training process within an hour, and stands out as the method with the fastest training speed compared to the baselines. We also report training results of our method on fully 5 cameras, for we use every forth frame of 5 cameras as our testing set, our performance dropped off slightly. Our rendering speed, measured in Frames Per Second (FPS), significantly outperforms competing methods and stands slightly below that of 3DGS [14].

Table 2. Novel view synthesis of static scenes on Waymo.

Methods	PSNR $\uparrow$	SSIM $\uparrow$	LPIPS $\downarrow$
S-NeRF [40]	23.60	0.743	0.422
StreetSurf [13]	21.49	0.771	0.412
3DGS [14]	24.08	0.807	0.322
PVG (Ours)	<b>25.31</b>	<b>0.812</b>	<b>0.304</b>

For static scenes, as shown in Table 2, we align with the settings in S-NeRF [40], employing all five cameras for

Table 3. Image reconstruction of static scenes on Waymo, using the same settings in StreetSurf [13].

Sequence	PSNR	
	StreetSurf	PVG (Ours)
seg1534950...	27.26	<b>28.10</b>
seg4058410...	28.08	<b>32.97</b>
seg3425716...	29.42	<b>30.45</b>
seg1347637...	28.20	<b>30.03</b>
Average	28.24	<b>30.39</b>

training and designating every fourth timestamp’s frame as the test set. The training sequences utilized are the same as those reported in S-NeRF[40]. Our model not only outperforms the baselines [13, 14, 40] which are focused on static scenes across three metrics but also demonstrates a discernible enhancement in image quality, as evidenced in Figure 5. To be more convinced, we conduct additional experiments using the same setup as in StreetSurf [13], using the randomly selected four sequences from the results reported in StreetSurf[13]. Our evaluation, focusing on PSNR, as StreetSurf only reports PSNR in their papers, reveals in Table 3 that our model achieves significant advancements over previous approaches dedicated to static scenes.

We also show that by making use of the 2D semantic labels provided in a video sequence, our method can derive semantic categories in novel viewpoints or timestamps as shown in Figure 6. This is achieved by assigning a 19-dimension vector for each Gaussian, representing the probability of which category the Gaussian belongs to and the rendered probability map is supervised by 2D semantic labels with cross-entropy.

**Results on KITTI** Our approach is also quantitatively evaluated on the KITTI benchmark, following SUDS [33]. We select sequences characterized by extensive movement for analysis. The proposed method surpasses all baseline methods across every evaluated metric. Notably, while these sequences present a substantial number of dynamic objects, our scene flow-based mechanism secures a concise

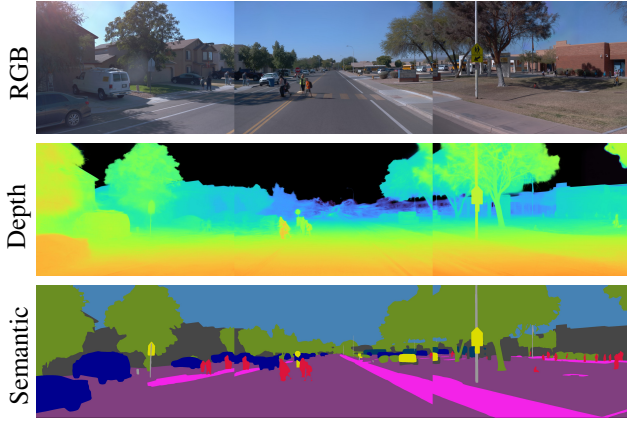


Figure 6. **Rendered rgb, depth and semantic label.** Supervised by 2D semantic labels from the given video sequence, PVG can learn each point a semantic label and can be rendered as above.

scene representation, thereby mitigating over-fitting and ensuring superior image quality in novel viewpoints. Table 1 demonstrates our significant improvement over the leading SUDS [33] baseline in image reconstruction, with improvements of 11.4% in PSNR, 5.8% in SSIM, and a 55.1% decrease in LPIPS and surpass the leading Mars [38] baseline in novel view synthesis with improvement of 9.9% in PSNR, 4.7% in SSIM, and a 20.6% decrease in LPIPS.

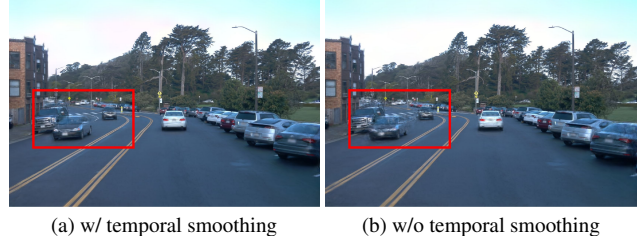
### 4.3. Ablation study

In Table 4, we conduct an ablation study to investigate the impact of the primary components of our model on novel view synthesis within dynamic scenes, specifically utilizing the Waymo Open Dataset. We set  $\eta = 1$  to deactivate the scene flow-based temporal smoothing mechanism, a crucial element in RGB rendering. As illustrated in Figure 7, the scene flow-based temporal smoothing mechanism results in enhanced smoothness in novel view rendering and promotes temporal and spatial consistency of PVG points. Our findings indicate that the integration of LiDAR supervision, sky refinement, and opacity loss contributes to more plausible geometry, albeit with a minimal effect on novel view RGB rendering. Unbounded-scene control strategy significantly improves the reconstruction of distant views. Additionally, the inclusion of velocity loss facilitates the convergence of velocity to a sparser rank, thereby simplifying the segmentation process between dynamic and static elements.

**Vibration vs. linear and stationary** We next investigate the influence of cycle length on our model. To this end, we conduct experiments across a range of cycle lengths  $l$  within the interval  $[0, \infty)$ . By maintaining a constant learning rate for  $\frac{2\pi\mathbf{A}}{l}$  and varying  $l$ , we observe a transition in the behavior of Gaussians from a tendency towards stasis to a linear motion. Specifically, at  $l = \infty$ , the motion of a

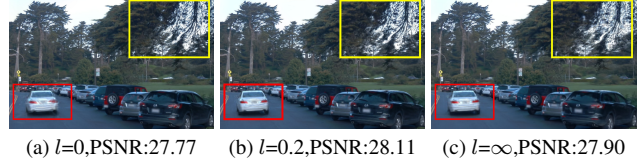
Table 4. Ablations on main components of our model.

	↑PSNR	↑SSIM	↓LPIPS
w/o temporal smoothing	26.50	0.805	0.315
w/o depth loss $\mathcal{L}_d$	28.10	0.849	0.279
w/o velocity loss $\mathcal{L}_v$	28.04	0.847	0.281
w/o opacity loss $\mathcal{L}_o$	28.11	0.848	0.280
w/o sky refinement and $\mathcal{L}_o$	28.01	0.846	0.278
w/o position-aware control	27.90	0.846	0.282
PVG (Ours)	<b>28.11</b>	<b>0.849</b>	<b>0.279</b>



(a) w/ temporal smoothing (b) w/o temporal smoothing

Figure 7. Ablation on temporal smoothing mechanism.



(a)  $l=0$ , PSNR:27.77 (b)  $l=0.2$ , PSNR:28.11 (c)  $l=\infty$ , PSNR:27.90

Figure 8. Ablation on cycle length  $l$ .

Gaussian becomes  $\tilde{\mu}(t) = \mu + vt$ . Conversely, at  $l = 0$ ,  $\tilde{\mu}(t)$  reduces to a constant value,  $\mu$ . As depicted in Figure 8, our findings reveal that models with excessively short cycle lengths adeptly represent static elements (highlighted in the yellow box) but exhibit suboptimal performance with dynamic elements (indicated in the red box). In contrast, models with extended cycle lengths more smoothly capture dynamic aspects. However, such models consistently misrepresent static components due to the difficulty in reducing the norm of  $v$  to zero, resulting in ambiguities and ghosting effects. We conclude that an optimal cycle length  $l$  is pivotal in achieving accurate reconstruction of both dynamic and static elements in the model.

## 5. Conclusion

We present the Periodic Vibration Gaussian (PVG), a model adept at capturing the diverse characteristics of various objects and materials within dynamic urban scenes in a unified formulation. By integrating periodic vibration, time-dependent opacity decay, and a scene flow-based temporal smoothing mechanism into the 3D Gaussian Splattering technique, we have established that our model significantly outperforms the state-of-the-art methods on the Waymo Open Dataset and KITTI benchmark, with significant efficiency advantage in dynamics scene reconstruction and novel view synthesis. While PVG excels in managing dynamic scenes,

it encounters limitations in precise geometric representation, attributable to its highly adaptable design. Future efforts will focus on improving geometric accuracy and further refining the model’s proficiency in accurately depicting the complexities of urban scenes.

## References

- [1] Jad Abou-Chakra, Feras Dayoub, and Niko Sünderhauf. Particlenet: Particle based encoding for online neural radiance fields in dynamic scenes. *arXiv preprint*, 2022. [2](#)
- [2] Benjamin Attal, Jia-Bin Huang, Christian Richardt, Michael Zollhoefer, Johannes Kopf, Matthew O’Toole, and Changil Kim. Hyperreal: High-fidelity 6-dof video with ray-conditioned sampling. In *CVPR*, 2023. [2](#)
- [3] Jonathan T Barron, Ben Mildenhall, Matthew Tancik, Peter Hedman, Ricardo Martin-Brualla, and Pratul P Srinivasan. Mip-nerf: A multiscale representation for anti-aliasing neural radiance fields. In *ICCV*, 2021. [2](#)
- [4] Jonathan T Barron, Ben Mildenhall, Dor Verbin, Pratul P Srinivasan, and Peter Hedman. Mip-nerf 360: Unbounded anti-aliased neural radiance fields. In *CVPR*, 2022.
- [5] Jonathan T Barron, Ben Mildenhall, Dor Verbin, Pratul P Srinivasan, and Peter Hedman. Zip-nerf: Anti-aliased grid-based neural radiance fields. *arXiv preprint*, 2023. [2](#)
- [6] Holger Caesar, Varun Bankiti, Alex H Lang, Sourabh Vora, Venice Erin Liong, Qiang Xu, Anush Krishnan, Yu Pan, Giacarlo Baldan, and Oscar Beijbom. nuscenes: A multimodal dataset for autonomous driving. In *CVPR*, 2020. [1](#)
- [7] Ang Cao and Justin Johnson. Hexplane: A fast representation for dynamic scenes. In *CVPR*, 2023. [2](#)
- [8] Anpei Chen, Zexiang Xu, Andreas Geiger, Jingyi Yu, and Hao Su. Tensorf: Tensorial radiance fields. In *ECCV*, 2022. [2](#)
- [9] Anpei Chen, Zexiang Xu, Xinyue Wei, Siyu Tang, Hao Su, and Andreas Geiger. Factor fields: A unified framework for neural fields and beyond. *arXiv preprint*, 2023. [2](#)
- [10] Zhiqin Chen, Thomas Funkhouser, Peter Hedman, and Andrea Tagliasacchi. Mobilenerf: Exploiting the polygon rasterization pipeline for efficient neural field rendering on mobile architectures. In *CVPR*, 2023. [2](#)
- [11] Sara Fridovich-Keil, Giacomo Meanti, Frederik Rahbæk Warburg, Benjamin Recht, and Angjoo Kanazawa. K-planes: Explicit radiance fields in space, time, and appearance. In *CVPR*, 2023. [2](#)
- [12] Andreas Geiger, Philip Lenz, and Raquel Urtasun. Are we ready for autonomous driving? the kitti vision benchmark suite. In *2012 IEEE conference on computer vision and pattern recognition*, 2012. [1, 2, 5](#)
- [13] Jianfei Guo, Nianchen Deng, Xinyang Li, Yeqi Bai, Botian Shi, Chiyu Wang, Chenjing Ding, Dongliang Wang, and Yikang Li. Streetsurf: Extending multi-view implicit surface reconstruction to street views. *arXiv preprint*, 2023. [1, 2, 5, 6, 7, 12, 13, 14, 15](#)
- [14] Bernhard Kerbl, Georgios Kopanas, Thomas Leimkühler, and George Drettakis. 3d gaussian splatting for real-time radiance field rendering. *ACM TOG*, 2023. [2, 3, 4, 5, 6, 7, 11, 12, 13, 14, 15](#)
- [15] Diederik P Kingma and Jimmy Ba. Adam: A method for stochastic optimization. *arXiv preprint*, 2014. [6](#)
- [16] Abhijit Kundu, Kyle Genova, Xiaoqi Yin, Alireza Fathi, Caroline Pantofaru, Leonidas J Guibas, Andrea Tagliasacchi, Frank Dellaert, and Thomas Funkhouser. Panoptic neural fields: A semantic object-aware neural scene representation. In *CVPR*, 2022. [1, 2](#)
- [17] Tianye Li, Mira Slavcheva, Michael Zollhoefer, Simon Green, Christoph Lassner, Changil Kim, Tanner Schmidt, Steven Lovegrove, Michael Goesele, Richard Newcombe, et al. Neural 3d video synthesis from multi-view video. In *CVPR*, 2022. [2](#)
- [18] Zhuopeng Li, Lu Li, and Jianke Zhu. Read: Large-scale neural scene rendering for autonomous driving. In *AAAI*, 2023. [2](#)
- [19] Jonathon Luiten, Georgios Kopanas, Bastian Leibe, and Deva Ramanan. Dynamic 3d gaussians: Tracking by persistent dynamic view synthesis. *arXiv preprint*, 2023. [2](#)
- [20] Ben Mildenhall, Pratul P Srinivasan, Matthew Tancik, Jonathan T Barron, Ravi Ramamoorthi, and Ren Ng. Nerf: Representing scenes as neural radiance fields for view synthesis. In *ECCV*, 2020. [2](#)
- [21] Thomas Müller, Alex Evans, Christoph Schied, and Alexander Keller. Instant neural graphics primitives with a multiresolution hash encoding. *ACM TOG*, 2022. [2](#)
- [22] Julian Ost, Fahim Mannan, Nils Thuerey, Julian Knodt, and Felix Heide. Neural scene graphs for dynamic scenes. In *CVPR*, 2021. [1, 2, 5, 6, 7, 12, 13, 14, 15](#)
- [23] Keunhong Park, Utkarsh Sinha, Jonathan T Barron, Sofien Bouaziz, Dan B Goldman, Steven M Seitz, and Ricardo Martin-Brualla. Nerfies: Deformable neural radiance fields. In *ICCV*, 2021. [2](#)
- [24] Keunhong Park, Utkarsh Sinha, Peter Hedman, Jonathan T Barron, Sofien Bouaziz, Dan B Goldman, Ricardo Martin-Brualla, and Steven M Seitz. Hypernerf: A higher-dimensional representation for topologically varying neural radiance fields. *arXiv preprint*, 2021.
- [25] Albert Pumarola, Enric Corona, Gerard Pons-Moll, and Francesc Moreno-Noguer. D-nerf: Neural radiance fields for dynamic scenes. In *CVPR*, 2021. [2](#)
- [26] Christian Reiser, Rick Szeliski, Dor Verbin, Pratul Srinivasan, Ben Mildenhall, Andreas Geiger, Jon Barron, and Peter Hedman. Merf: Memory-efficient radiance fields for real-time view synthesis in unbounded scenes. *ACM TOG*, 2023. [2](#)
- [27] Konstantinos Rematas, Andrew Liu, Pratul P Srinivasan, Jonathan T Barron, Andrea Tagliasacchi, Thomas Funkhouser, and Vittorio Ferrari. Urban radiance fields. In *CVPR*, 2022. [1, 2](#)
- [28] Cheng Sun, Min Sun, and Hwann-Tzong Chen. Direct voxel grid optimization: Super-fast convergence for radiance fields reconstruction. In *CVPR*, 2022. [2](#)
- [29] Pei Sun, Henrik Kretzschmar, Xerxes Dotiwalla, Aurelien Chouard, Vijaysai Patnaik, Paul Tsui, James Guo, Yin Zhou, Yuning Chai, Benjamin Caine, et al. Scalability in perception for autonomous driving: Waymo open dataset. In *CVPR*, 2020. [1, 2, 5](#)

- [30] Matthew Tancik, Vincent Casser, Xinchen Yan, Sabeek Pradhan, Ben Mildenhall, Pratul P Srinivasan, Jonathan T Barron, and Henrik Kretzschmar. Block-nerf: Scalable large scene neural view synthesis. In *CVPR*, 2022. 2
- [31] Edgar Tretschk, Ayush Tewari, Vladislav Golyanik, Michael Zollhöfer, Christoph Lassner, and Christian Theobalt. Non-rigid neural radiance fields: Reconstruction and novel view synthesis of a dynamic scene from monocular video. In *ICCV*, 2021. 2
- [32] Haithem Turki, Deva Ramanan, and Mahadev Satyanarayanan. Mega-nerf: Scalable construction of large-scale nerfs for virtual fly-throughs. In *CVPR*, 2022. 2
- [33] Haithem Turki, Jason Y Zhang, Francesco Ferroni, and Deva Ramanan. Suds: Scalable urban dynamic scenes. In *CVPR*, 2023. 1, 2, 5, 6, 7, 8, 11, 12, 13, 14, 15
- [34] Dor Verbin, Peter Hedman, Ben Mildenhall, Todd Zickler, Jonathan T Barron, and Pratul P Srinivasan. Ref-nerf: Structured view-dependent appearance for neural radiance fields. In *CVPR*, 2022. 2
- [35] Feng Wang, Sinan Tan, Xinghang Li, Zeyue Tian, Yafei Song, and Huaping Liu. Mixed neural voxels for fast multi-view video synthesis. In *ICCV*, 2023. 2
- [36] Zian Wang, Tianchang Shen, Jun Gao, Shengyu Huang, Jacob Munkberg, Jon Hasselgren, Zan Gojcic, Wenzheng Chen, and Sanja Fidler. Neural fields meet explicit geometric representations for inverse rendering of urban scenes. In *CVPR*, 2023. 2
- [37] Guanjun Wu, Taoran Yi, Jiemin Fang, Lingxi Xie, Xiaopeng Zhang, Wei Wei, Wenyu Liu, Qi Tian, and Xinggang Wang. 4d gaussian splatting for real-time dynamic scene rendering. *arXiv preprint*, 2023. 2
- [38] Zirui Wu, Tianyu Liu, Liyi Luo, Zhide Zhong, Jianteng Chen, Hongmin Xiao, Chao Hou, Haozhe Lou, Yuantao Chen, Runyi Yang, et al. Mars: An instance-aware, modular and realistic simulator for autonomous driving. *arXiv preprint*, 2023. 2, 5, 6, 7, 8, 12, 13, 14, 15
- [39] Enze Xie, Wenhui Wang, Zhiding Yu, Anima Anandkumar, Jose M Alvarez, and Ping Luo. Segformer: Simple and efficient design for semantic segmentation with transformers. *NeurIPS*, 2021. 5
- [40] Ziyang Xie, Junge Zhang, Wenye Li, Feihu Zhang, and Li Zhang. S-nerf: Neural radiance fields for street views. In *ICLR*, 2022. 1, 2, 5, 6, 7, 12, 13, 14, 15
- [41] Ze Yang, Yun Chen, Jingkang Wang, Sivabalan Manivasagam, Wei-Chiu Ma, Anqi Joyce Yang, and Raquel Urtasun. Unisim: A neural closed-loop sensor simulator. In *CVPR*. 2
- [42] Lior Yariv, Peter Hedman, Christian Reiser, Dor Verbin, Pratul P Srinivasan, Richard Szeliski, Jonathan T Barron, and Ben Mildenhall. Bakedsdf: Meshing neural sdfs for real-time view synthesis. *arXiv preprint*, 2023. 2

# Appendices

## A. More model interpretation

**Our representation model** To facilitate understanding how our proposed PVG model functions, we consider a simplified scene with both static and dynamic components, as illustrated in Figure 9. Concretely, PVG points with long lifespans are used for quantifying static scene elements as the conventional 3D Gaussian counterpart, whilst those with short lifespans distributed over space and time for representing the unconstrained dynamic components of a scene.

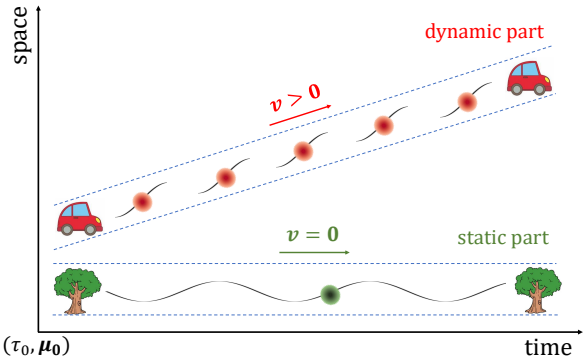


Figure 9. Consider a 4D space-time coordinate system with a non-zero slope for dynamic objects and zero slope for the static. Every PVG point’s trajectory is characterized by a piecewise sine function with specific domain of definition and amplitude. PVG points with small staticness coefficient  $\rho$  (red points) and short lifespans learn to model dynamic scene parts, alongside those with large  $\rho$  (green points) and long lifespans for explaining static scene parts. To represent unconstrained motion (e.g., moving car), a collection of PVG points will work out in a cohort.

**Scene flow-based temporal smoothing** Due to sparse training frames, the renderings of novel timestamps are prone to underfitting. To render the  $\{\mathcal{H}_i\}$  temporally and spatially consistent with its scene flow velocity, we exploit the inherent temporal consistency law: The status  $\mathcal{H}_i(t)$  at time  $t$  is similar to the result  $\hat{\mathcal{H}}_i(t)$  of translating the status at  $t - \Delta t$  by a distance  $v\Delta t$ . This introduces an additional optimization regularization defined as:

$$\min \mathbb{E}_{t, \Delta t} \text{Diff}(\{\mathcal{H}_i(t)\}, \{\hat{\mathcal{H}}_i(t)\}), \quad (13)$$

where  $\text{Diff}(\cdot)$  is a difference measurement about two set of 3D Gaussian points. While it is hard for us to directly calculate  $\text{Diff}(\cdot)$ , we use an indirect measurement by rendering function  $\text{Render}(\cdot)$ .

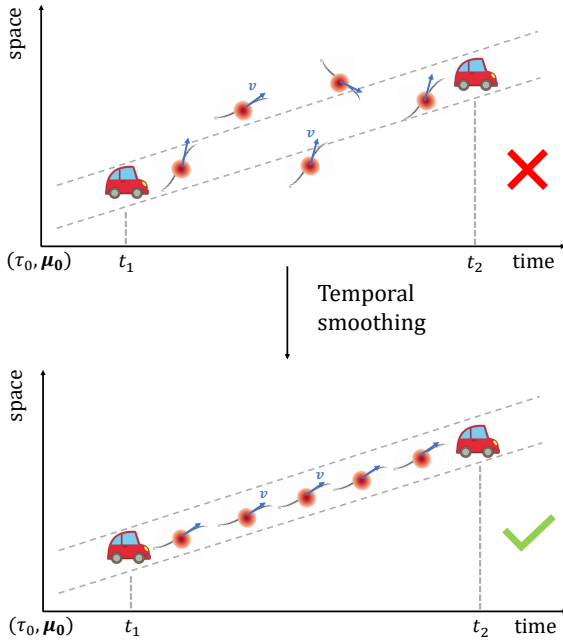


Figure 10. Consider two adjacent training frames with timestamp  $t_1$  and  $t_2$  (a small time window). In a small time period, we assume dynamic objects move linearly. At observed times  $t_1$  and  $t_2$ , RGB renderings could fit well. However for the moments in between ( $t_1 < t_b < t_2$ ), we have no corresponding training data to constrain our model  $\{\mathcal{H}_i(t_b)\}$ . To prevent our model from behaving improperly, we impose a smooth constraint subject to the slope of  $v$ . The frames used to train are knots of a function, what we need to do is making the knots more smoothly connected.

Our final objective function could be written as the expectation form of the differences between two ways of rendering:

$$\min_{\mathbf{E}, \Delta t, \mathbf{E}, \mathbf{I}} \|\text{Render}(\{\mathcal{H}_i(t)\}) - \text{Render}(\{\hat{\mathcal{H}}_i(t)\})\|, \quad (14)$$

for any camera extrinsic  $\mathbf{E}$  and intrinsic  $\mathbf{I}$ , timestamp  $t$  and small time shift  $\Delta t$  (the camera pose and time parameter in  $\text{Render}(\cdot)$  function are omitted for simplicity).

To compute Eq. (14), we need to render twice, making sampling every camera pose and timestamp computationally expensive. For efficiency, in practice we sample  $\{t, \mathbf{E}, \mathbf{I}\}$  uniformly from the training set and sample  $\Delta t$  from  $U(-\delta, +\delta)$ , and replace  $\text{Render}(\{\mathcal{H}_i(t)\})$  with the ground truth image to only render once for every step. Figure 10 shows a more vivid illustration of the temporal smoothing mechanism.

## B. Visualization for Waymo

More novel view synthesis results are in Figure 12 and Figure 13. We project the LiDAR points to the camera world as

the ground truth depth map. SUDS [33] is good at image reconstruction, but poor at novel view synthesis. 3DGS [14] is only good for static and close-range reconstruction but unable to handle distance view and dynamic objects. In contrast, our method can not only reconstruct both the near and distance well, but also render images with the quality as the ground-truth.

## C. Visualization for KITTI

The scenarios of KITTI used in [33] are almost the scenarios where the ego vehicle is not moving. The quality of depth reconstruction depends on the point cloud. Image reconstruction results and novel view synthesis results are in Figure 14 and Figure 15.

## D. Velocity map and $\rho$ map

We visualize the renderings of velocity map  $\mathcal{V}$  and  $\rho$  map to analyze the behavior of PVG. For the visualization of  $\mathcal{V}$ , we first transform  $v$  of each pixel from the world coordinate system to the camera coordinate system and project the  $v_{cam}$  onto a plane parallel to the camera plane. Then we use the color coding of optical flow for visualization.

For the visualization of  $\rho$  map, we need to clamp each point's  $\rho$  to the range of  $[0, 2]$ , otherwise the visualization is not visually distinctive.

As shown in Figure 11, our model captures not only dynamic objects like cars and people, but also moving light and shadow. Note pixels with small  $\rho$  point to dynamic areas and the left for static ones.

## E. Limitation

Unlike neural network based representation models, our PVG uses independent and discrete points to represent scenes. Despite the advantages including high flexibility, simple composition, strong expression ability, and strong fitting ability, the independence of each point makes it more difficult to model the smoothness over time and space. Our temporal smoothing mechanism does enhance the correlation between points, but still not fully solves this problem. More fine-grained design are needed for further enhancement.

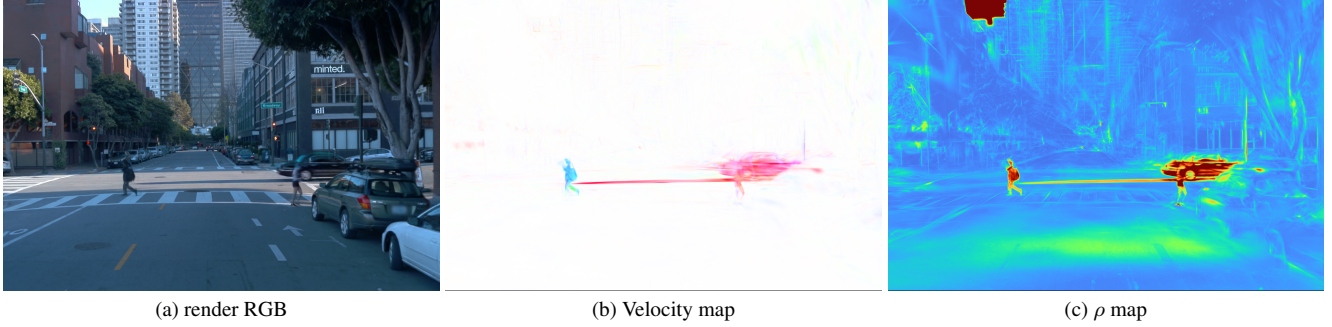


Figure 11. Visualization of (b) the velocity map and (c)  $\rho$  map of (a) a scene with a left-to-right moving car and two walking pedestrians. It is evident that our model captures the motion, dynamic (including even the car's shadow) and static parts of the scene. Blue/red: Large/small  $\rho$  pointing to static/dynamic areas.

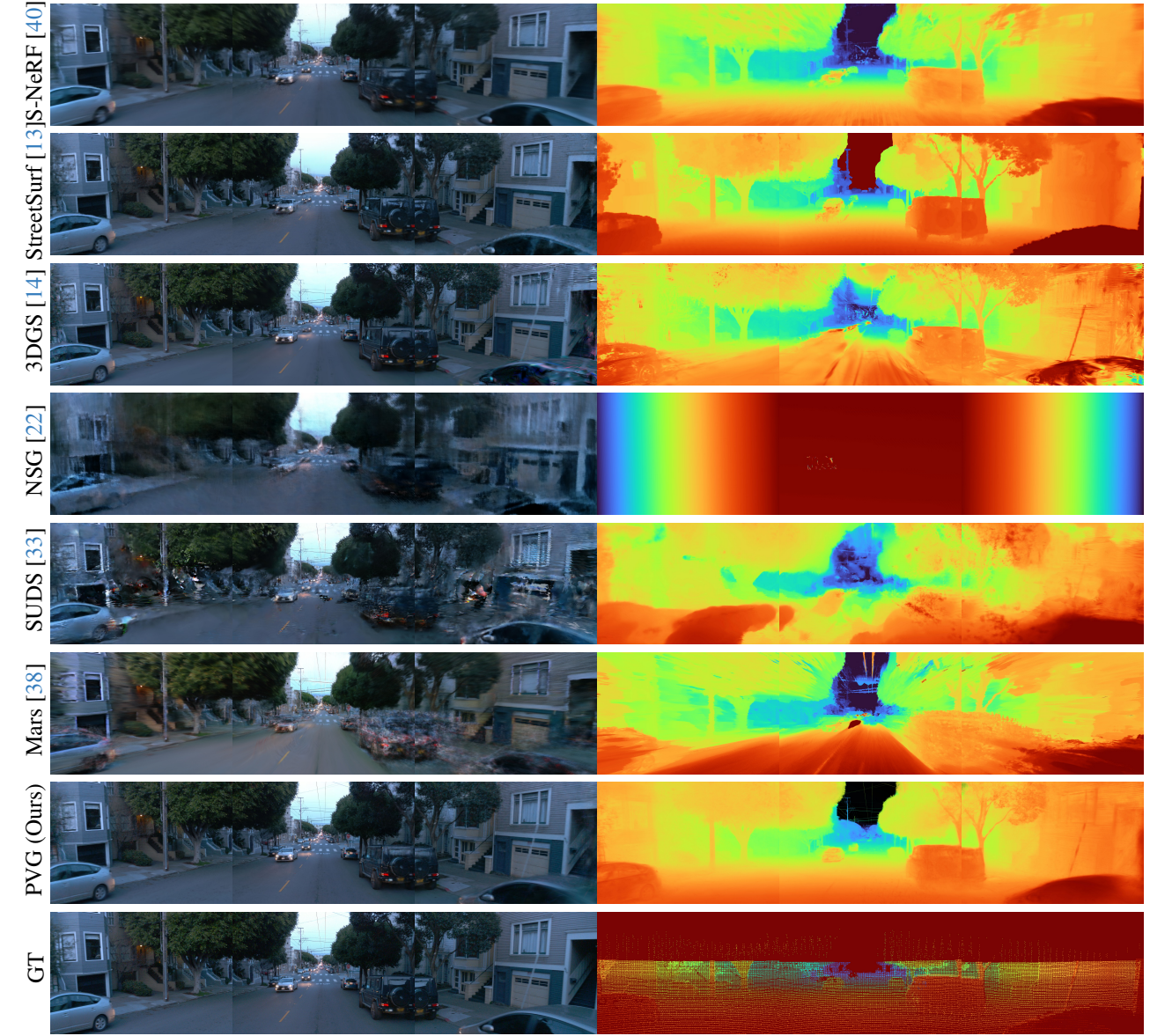


Figure 12. Qualitative results of novel view synthesis on Waymo. GT: Ground-truth.

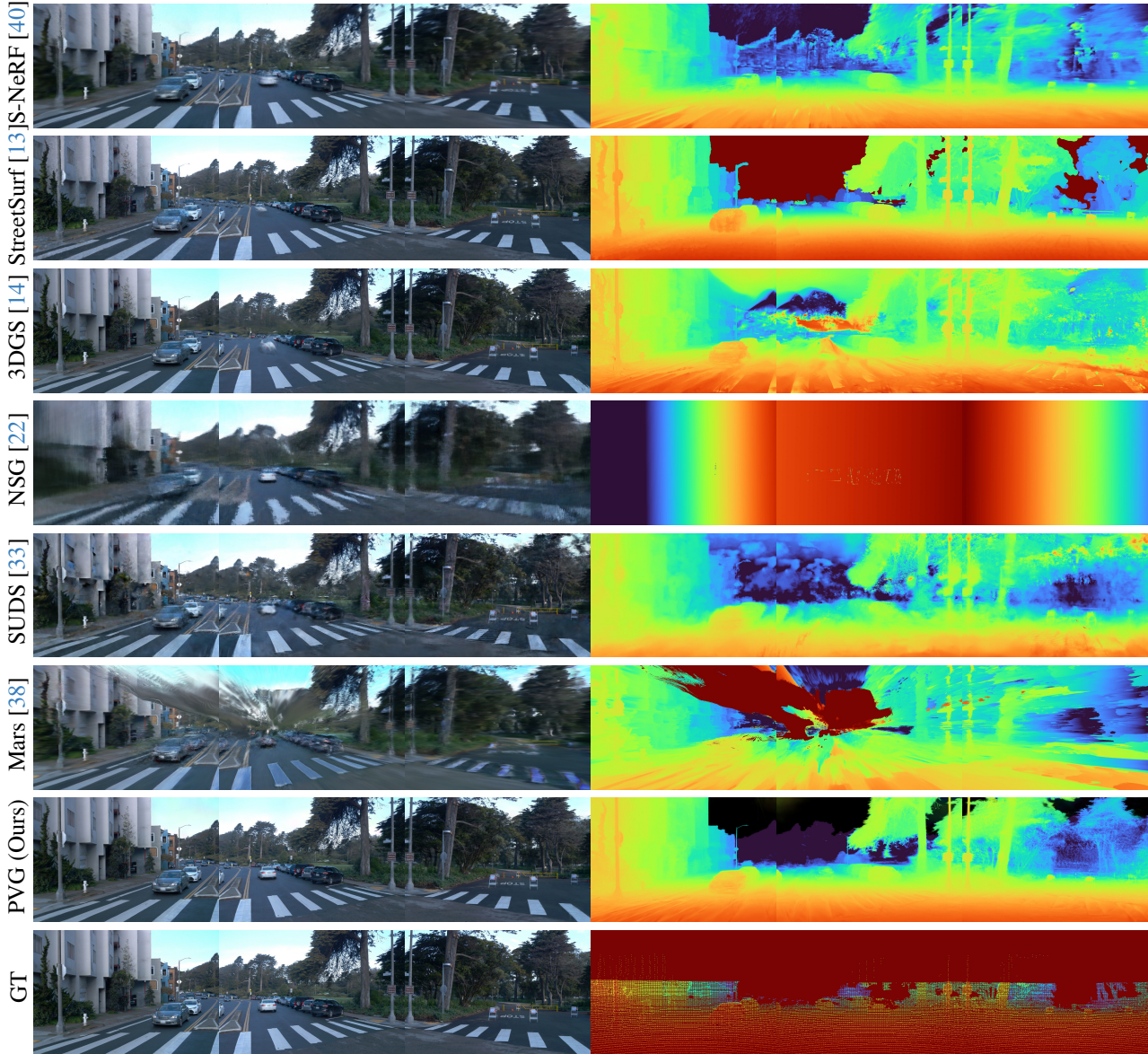


Figure 13. Qualitative results of novel view synthesis on Waymo.

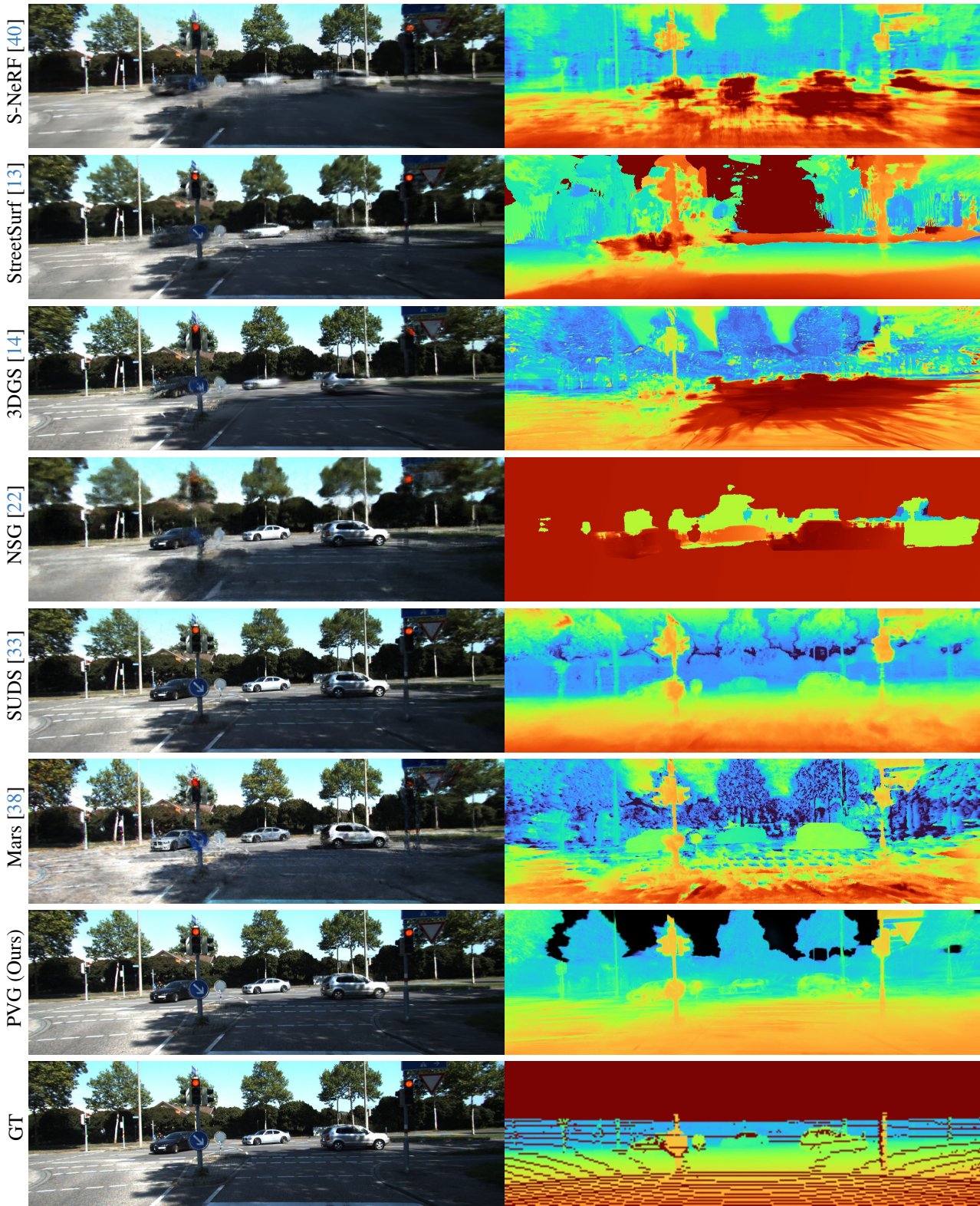


Figure 14. Qualitative results of image reconstruction on KITTI.

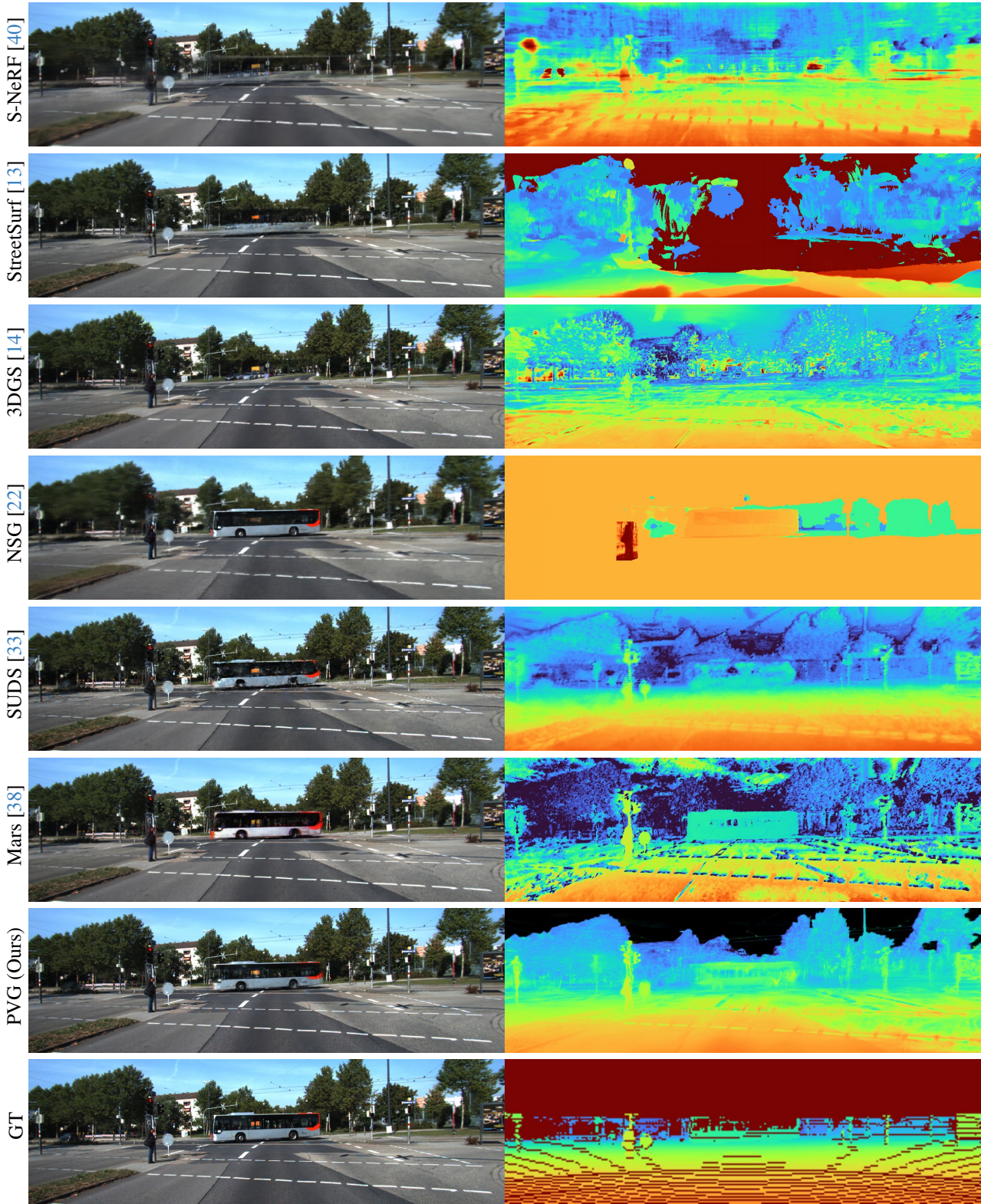


Figure 15. Qualitative results of novel view synthesis on KITTI.